

Frequency clusters and defect structures in nonlinear dust-density waves under microgravity conditions

K. O. Menzel,* O. Arp, and A. Piel

Institut für Experimentelle und Angewandte Physik, Christian-Albrechts-Universität, D-24098 Kiel, Germany

(Received 22 October 2010; revised manuscript received 24 November 2010; published 18 January 2011)

Density waves in a dusty plasma emerge spontaneously at low gas pressures and high dust densities. These acousticlike wave modes were studied in a radio-frequency discharge under microgravity conditions. The complex three-dimensional wave pattern shows a spatially varying wavelength that leads to bifurcations, i.e., topological defects, where wave fronts split or merge. The calculation of instantaneous wave attributes from the spatiotemporal evolution of the dust density allows a precise analysis of those structures. Investigations of the spatial frequency distribution inside the wave field revealed that the wave frequency decreases from the bulk to the edge of the cloud in terms of frequency jumps. Between those jumps, regions of almost constant frequency appear. The formation of frequency clusters is strongly correlated with defects that occur exclusively at the cluster boundaries. It is shown that the nonlinearity of the waves has a significant influence on the topology of the wave pattern.

DOI: [10.1103/PhysRevE.83.016402](https://doi.org/10.1103/PhysRevE.83.016402)

PACS number(s): 52.27.Lw, 52.35.Mw, 52.35.Fp, 05.45.Xt

I. INTRODUCTION

A dusty (complex) plasma contains—besides ions, electrons, and neutrals—micrometer sized particles. This fourth, heavy component shows various structures and dynamic phenomena that take place on comparably long time scales, since the characteristic dust-plasma frequency is of the order of only a few ten Hz. This makes the oscillatory motion of the particles easily accessible via standard video cameras in experiments. Since the first observation of a spontaneously emerging dust-acoustic-like wave mode in dusty plasmas [1], dust-density waves (DDWs) are of fundamental interest in this field of research. Experiments on DDWs were performed in direct current (dc) [2–7], as well as in radio-frequency (rf) discharges [8–11]. In laboratory experiments, the dust particles sediment into the plasma sheath because of gravity. Experiments with spatially extended dust clouds were carried out under microgravity conditions during parabolic flights [10,11] and aboard the International Space Station (ISS) [12,13]. As self-excited dust-density waves are attributed to a Buneman-type instability, where the input of free energy to the system is generated by streaming ions [14], its onset critically depends on three plasma parameters, namely the gas pressure, the discharge electric field, and the dust density [11].

In the last few years, experimental investigations with emphasis on nonlinear wave phenomena became of high interest [15]. Reports included the observation of nonlinear, periodic waves in the laboratory [16] and under microgravity [17]. In addition, the interaction of dust-acoustic shock waves was investigated in a glow discharge [18]. On the microscopic level, wave breaking inside DDWs was observed [9]. A recent investigation showed a strong modulation of the plasma glow by the DDWs in microgravity experiments, suggesting a nonlinear interaction between plasma and wave [19].

On the theoretical side, dust-acoustic waves were originally predicted in 1990 by Rao *et al.* [20]. A fluid model was used to explain a dust-acoustic instability, resulting in a linear dispersion relation and a Korteweg–de Vries equation

for the nonlinear case. Through the years, several further approaches were introduced. They include fluid as well as kinetic models and take into account dust-ion collisions [14,21], dust-density inhomogeneities [22], and grain charge variations [23–25]. Those improvements allow reasonable predictions of wavelengths, frequencies, and growth rates. In addition, a two-dimensional treatment of streaming ions gives local growth rates with respect to the ion velocity and can therefore explain the existence of an oblique mode arising under microgravity conditions [10,11,14].

In order to measure the dispersion properties of DDWs, the temporal modulation of plasma parameters is a widely used approach. For example, Thompson *et al.* [2] applied an additional low-frequency electric field to the discharge, resulting in a synchronization of driving force and oscillating dust density. This method allowed the verification of most of the wave properties that were predicted from linear theories. The entrainment process itself was lately studied in detail [26].

Recently, we discovered under microgravity conditions [27] that regions of different but almost constant frequency occur in the dust-density wave fields, so-called frequency clusters. This feature is accompanied by the appearance of topological defects. In this paper, we refine the previous analysis and describe the observed features in more detail. Moreover, we address the role of defects on the formation of frequency clusters. A comparison of the findings with numerical simulations suggests a model for our system, which explicitly accounts for the nonlinear wave character.

II. EXPERIMENTAL SETUP

The measurements were performed under microgravity conditions on parabolic flights provided by DLR (German Aerospace Center). The waves were generated in the IMPF-K2 chamber, which is an improved descendant of the chamber prototype for the International Plasma Microgravity Facility (IMPF). It is similar to the facility described in detail in Ref. [28], except for a simplified electrode configuration.

A side view of the experimental setup is shown in Fig. 1(a). An argon plasma is produced by a symmetric parallel

*menzel@physik.uni-kiel.de

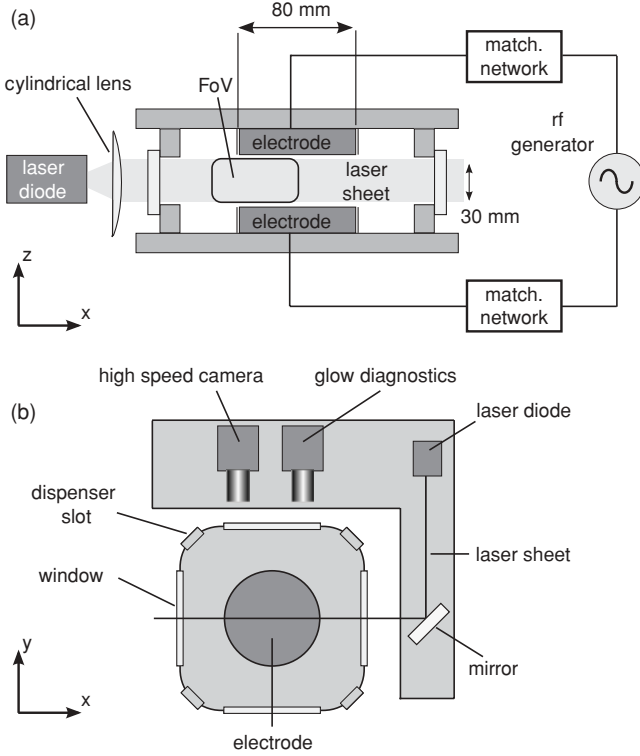


FIG. 1. Sketch of the IMPF-K2 chamber. (a) Side view of the chamber. The field of view is marked with a rectangle. (b) The top view shows the basic video microscopy setup with illumination laser and high speed camera.

plate radio-frequency discharge operated at 13.56 MHz. Two transparent electrodes made of indium tin oxide (ITO) with a diameter of 80 mm form a discharge gap of 30 mm and are fed in push-pull mode via a symmetric matching network by an rf generator with typical peak-to-peak voltages of $U_{rf} = (40-70) V_{pp}$.

Dust particles are injected into the plasma by eight independently operating dispensers. For the present investigations, this configuration ensures a high total amount of dust. The monodisperse and spherical melamin-formaldehyde particles have a diameter of $d = (6.84 \pm 0.07) \mu\text{m}$.

In this setup, self-excited DDWs can be observed only when the energy gain of the ions is sufficiently higher than dissipation arising from neutral drag. Consequently, in our experiment the gas pressure $p = (15-30) \text{ Pa}$ is chosen below a critical value of $p_{crit} \approx 35 \text{ Pa}$ to ensure the appearance of wave motion. To exclude the possibility that the observed instability is triggered by external mechanical forces, which may arise from residual gravity during the parabolic maneuver, an additional accelerometer was installed close to the plasma chamber that logs the acceleration in all three spatial directions at a sample rate of 1 kHz.

For the observation of the dust dynamics, a standard video microscope was used. The configuration, as seen in Fig. 1(b), comprises a low-power laser diode ($\lambda = 660 \text{ nm}$, 50 mW) that illuminates the dust particles with a thin vertical sheet and a high speed camera. By choosing a frame rate of approximately 100 fps we can exclude any aliasing effects in the recorded wave motion as the frequency of the DDWs is typically only

of the order of a few Hz. The observed field of view (FOV) has a spatial resolution of (510×880) pixels, corresponding to an area of $(25 \times 43) \text{ mm}^2$ inside the laser sheet.

III. FUNDAMENTAL WAVE PROPERTIES

A characteristic snapshot of the dust cloud is shown in Fig. 2(a). It was recorded at $U_{rf} = 65 V_{pp}$ and $p = 30 \text{ Pa}$. Typically, the dust fills a large volume of the discharge except for the central dust-free void region [29]. For the given set of parameters, the dust density is obviously periodically

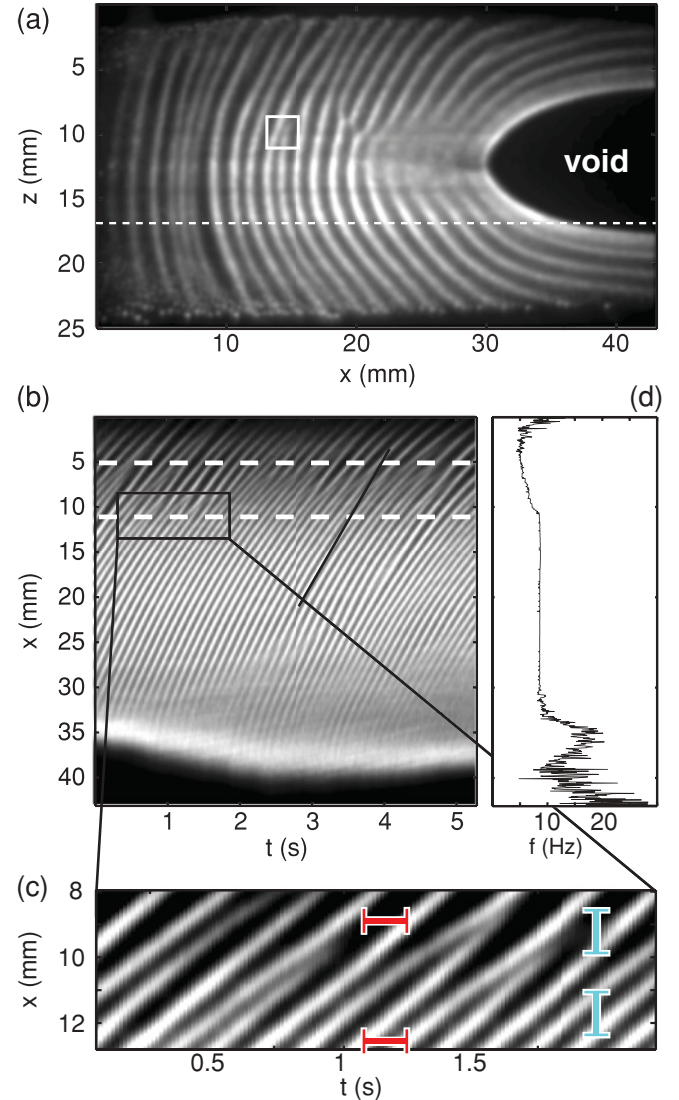


FIG. 2. (Color online) (a) Typical snapshot of the wave field in the rf discharge. Topological defects are merging points of two wave fronts (square). They develop in the bulk region of the dust cloud. (b) Space-time diagram for the dashed line in (a). The added black line demonstrates that waves with different phase velocity exist. Wave fronts merge at distinct bifurcation points in a region between the dashed lines. (c) A closeup shows the vicinity of several defects. The red (horizontal) and blue (vertical) bars of equal length match the wave field in the lower part but deviate in the upper part. (d) Spatial frequency distribution along the dashed line, determined from the maxima and minima of the space-time diagram.

modulated by self-excited DDWs. The waves are not generated by a periodically expanding and collapsing void boundary, associated with the heartbeat instability [30]. This can be concluded since the waves initially emerge at the outer parts of the dust clouds near the discharge edges when the gas pressure is lowered successively and falls below the critical pressure. For a further decrease, the wave field then expands over the entire cloud. Moreover, by checking the recorded acceleration, we can exclude any correlation between residual acceleration inside the aircraft and the dust-density fluctuations. The waves propagate radially outward from the boundary of the void. Although the waves gain energy from streaming ions, it is known from earlier experiments [10,11] that the waves do not necessarily propagate parallel to the local ion flow and the electric field, respectively.

Because the electric field is perpendicular to the plasma edge, one would expect that the waves strike the discharge edges at right angles. This is only true in the vicinity of the void, but may be different in the outer regions [10,11]. The snapshot further reveals the nonlinear character of the DDWs: The waves consist of very narrow crests and wide troughs, which contain a significantly reduced number of dust particles. Furthermore, it becomes obvious that the wavelength varies over the entire dust cloud with typical values of $\lambda_{DDW} \approx 1.5$ mm close to the void and $\lambda_{DDW} \approx 3$ mm in the outer regions of the cloud. We also observed that wave fronts are not strictly parallel, but they may split or merge spontaneously. Such spots are known as topological defects.

A first impression of the temporal behavior of the waves can be obtained from a space-time diagram as displayed in Fig. 2(b). It transforms the intensity evolution along a chosen horizontal section [dashed line in Fig. 2(a)] into a two-dimensional map, where the abscissa represents time and the ordinate represents the horizontal position. This method was already established in the context of DDW analysis [16,17,26] and allows us to determine several wave properties, e.g., phase velocity, wavelength, and wave period, as it is possible to track single wave fronts over time.

The local phase velocity of the DDW is represented by the slope of a wave front. In the diagram of Fig. 2(b) the black line of constant slope indicates that the velocity is decreasing toward the dust cloud edge, since the wave slope bends away from the line in the upper part of the diagram. Velocities of 15 mm s^{-1} in the dust volume and 8 mm s^{-1} near the boundary were obtained.

A change in frequency and wavelength can be seen by the red (horizontal) and blue (vertical) bars of identical length in Fig. 2(c), which match the wave field in the lower region but reveal a mismatch in the upper region. One generally finds higher frequencies near the void. This is an important finding, since it cannot be understood within the context of linear wave theory that would require a fixed frequency and would only allow a spatial variation of the wavelength.

The closeup view in Fig. 2(c) presents a case where pairs of wave fronts merge, resulting in one single wave front. This demonstrates that a topological defect is not only a spatial phenomenon but must be treated also in the time domain. Figure 2(b) clearly shows that such events are not equally distributed along the chosen axis. Rather, the defects occur inside a band that is marked by dashed lines.

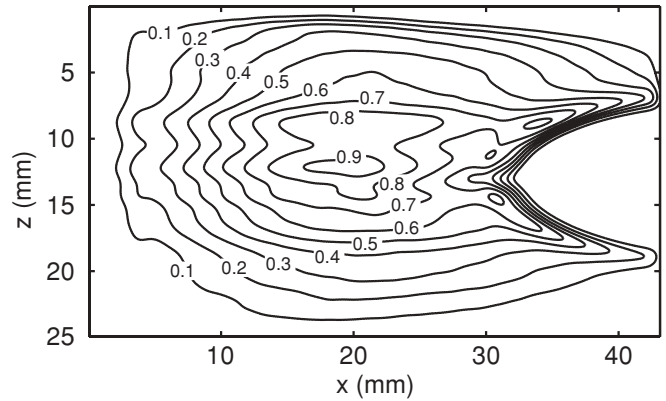


FIG. 3. Dust-density distribution for the wave field of Fig. 2(a). The density is given in arbitrary units, normalized to the maximum of the distribution. A strong gradient from the void boundary toward the discharge edges is established. Ripples in the density contours are caused by inhomogeneous illumination.

Since the distance between two wave fronts determines the wave period and frequency, respectively, it is possible to estimate a spatial frequency distribution along the axis by averaging over the distance between neighboring maxima and minima, respectively. The resulting distribution for a time series of 200 frames at constant plasma parameters is displayed in Fig. 2(d). It reveals a constant frequency over a broad region (11–30 mm) and the expected decrease toward the discharge edge. In the region of low wave activity (30–35 mm), the frequency estimation yields spurious values.

A qualitative picture of the dust-density distribution inside the dust cloud can be obtained by averaging the recorded intensity over an appropriate time interval. The result for the measurement of Fig. 2(a) is displayed in Fig. 3. It is found that the density is not constant over the entire cloud but decreases gradually from the void to the discharge edges.

IV. FREQUENCY CLUSTERS

As mentioned earlier, the spatial frequency variation of the DDW is not a trivial finding. It is rather associated to the complicated topology of the nonlinear wave field. Hence it is important to determine the spatial frequency distribution for the entire wave field.

A. Data processing

This is done by evaluating the time series of the dust-density evolution everywhere in the wave field. It is common to use the recorded intensity of the video frames as a direct measure of the density. All effects that may result from the granularity of particles are suppressed by blurring single frames with a Gaussian low-pass filter. This yields the individual time series $n_d(x, z, t)$ for the dust density at an arbitrary pixel position, denoted by spatial coordinates (x, z) . The time series have a length of 512 time steps and are made zero mean by subtracting a moving average. After such data preprocessing, the typical evolution of the dust density can be found in Fig. 4(a). The envelope function, defined from the instantaneous wave amplitude (see below), decreases between two maxima, which hints at interference phenomena. When investigating the

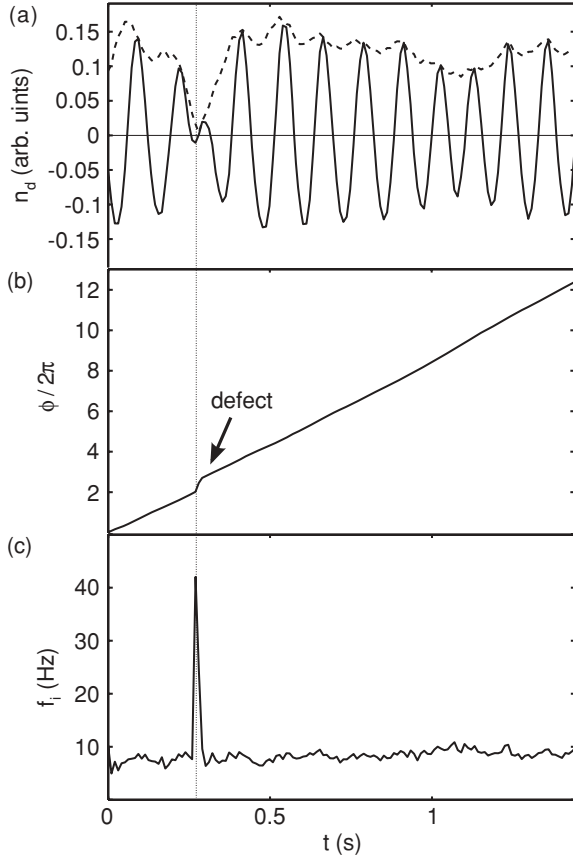


FIG. 4. (a) Measured zero-mean time series of the dust-density fluctuations for one distinct position in the dust cloud. The instantaneous amplitude is marked with a dashed line. Its sudden drop to zero indicates the occurrence of a topological defect. (b) Unwrapped phase information for the same position in the wave field shows an abrupt jump by π at the defect. (c) Instantaneous frequency for the same position, determined by the slope of the phase evolution. The dotted vertical line in the three graphs indicates the moment of defect occurrence.

envelope over several wave periods, it becomes obvious that the system is nonstationary.

The next step of the analysis is to determine the instantaneous frequency of the wave from a given time series. For this purpose, we expand the measured real time series into the complex plane via

$$A(x, z, t) = n_d(x, z, t) + i\hat{n}_d(x, z, t). \quad (1)$$

The resulting time series $A(t)$ is known as the “analytic signal,” first introduced by Gabor [31], and represents a standard technique in digital signal processing. It consists of the original time series and an additional imaginary part, which is calculated by the Hilbert transform $H\{n_d(t)\}$, defined as

$$\hat{n}_d(t) = H\{n_d(t)\} = \frac{1}{\pi} \int_{-\infty}^{\infty} \frac{n_d(\tau)}{t - \tau} d\tau. \quad (2)$$

Transferring Eq. (1) into Euler’s notation clearly shows the advantage of this expression, since $A(x, z, t) = E(x, z, t) \cdot$

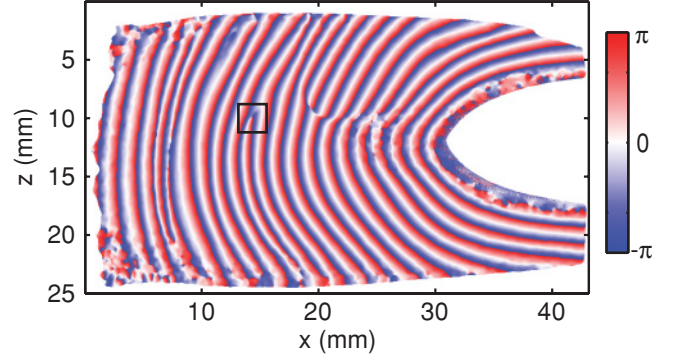


FIG. 5. (Color online) Calculated instantaneous phase for the same time step as in Fig. 2(a). Pixels with no wave activity were neglected and set to zero. Although the raw image shows almost no wave activity at the left edge of the void, phase fronts can be reconstructed in this area, indicating a correlation between upper and lower parts of the dust cloud.

$\exp[i \cdot \phi(x, z, t)]$ with the envelope function $E(x, z, t) = (n_d^2 + \hat{n}_d^2)^{1/2}$ gives rise to the definition of an instantaneous phase,

$$\phi(x, z, t) = \text{atan2}[\hat{n}_d(x, z, t), n_d(x, z, t)]. \quad (3)$$

The spatial phase distribution for the snapshot of Fig. 2(a) is illustrated in Fig. 5. It clearly reproduces the shape of the wave fronts. Moreover, it reveals wave motion in a region, where no waves could be visually detected in the raw data. The representation further demonstrates that the parts above and below the void show correlation, although the wave fronts between them are not connected.

The described methodological approach is widely used in numerous different research areas, as, for example, in biological, medical, and nonlinear physical systems [32], mainly due to the fact that $\phi(x, z, t)$ can be utilized to generate two more physical quantities that are of interest, namely the instantaneous frequency, defined as $f_i(t_0) = (1/2\pi) \cdot \partial\phi/\partial t|_{t=t_0}$, and the local wave vector, defined as $\vec{k}_l(\vec{r}_0) = \partial\phi/\partial\vec{r}|_{\vec{r}=\vec{r}_0}$.

Usually the phase lies between 0 and 2π . In contrast, Fig. 4(b) displays the temporal evolution of the unwrapped phase where all eventual phase jumps $2\pi \rightarrow 0$ are unfolded. It was determined at the same position as the time series of Fig. 4(a). One can see that $\phi(t)$ is in general a monotonically increasing function. Exceptions are at some distinct time steps. They are clear hints for the appearance of a defect, as will be seen in Sec. V. The slope of the phase evolution at a selected time step t_0 , representing the instantaneous frequency, can be seen in Fig. 4(c). It varies only slightly, except for defect positions. We thus define the time-averaged frequency $f_m = \langle f_i(t) \rangle_T$. The averaging time T is chosen according to the specific purpose of the data analysis. No averaging yields instantaneous properties. Averaging over one wave period (≈ 10 – 20 frames) improves the signal-to-noise ratio. Averaging over several wave periods (> 100 frames) is used to evaluate global wave properties when the plasma conditions are constant and the system parameters are not affected by residual gravity.

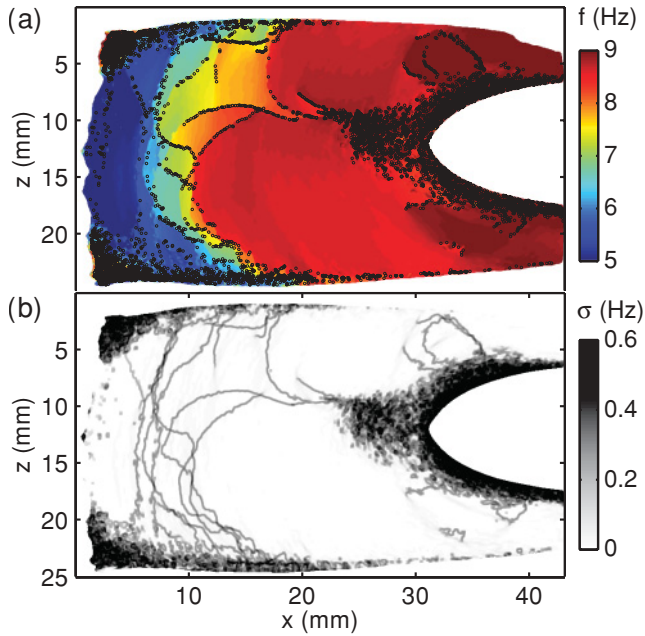


FIG. 6. (Color online) (a) Spatial frequency distribution for the same field of view as in Fig. 2(a), calculated via Hilbert transform. Different regions of nearly constant frequencies established in the wave field. The topological defects that encircle single frequency clusters are marked with black dots. (b) Standard deviation of the frequency distribution in a (5×5) pixel vicinity of each spot. Pixels with no wave activity were removed from both maps.

B. Frequency distributions

If the described procedure is carried out for all positions of the recorded two-dimensional dust volume sections, a spatial frequency distribution $f_m(x, z)$ can be constructed. The map in Fig. 6(a) results from the evaluation of time series of about 10–20 wave periods (200 frames). As immediately seen, the frequency is not constant in the dust cloud. It rather decreases from 8.6 Hz at the void edge to 5.2 Hz at the plasma boundary by roughly 40%. The waves always propagate in the direction of lower frequencies. In addition, the frequency decays nonmonotonically. Moreover, we find regions of almost constant frequency that are separated by significant frequency jumps. These regions are called frequency clusters. For the largest clusters, average frequencies of $f_1 = 5.2$ Hz, $f_2 = 7.8$ Hz, and $f_3 = 8.6$ Hz were determined. Inside those regions the frequency stays nearly constant with maximum deviations of about 4%. The mentioned features are even more pronounced in a horizontal section through the frequency distribution (Fig. 7) where the distributions obtained from the space-time diagram (fine black line) are compared with the Hilbert transform (bold red line) for the axis marked in Fig. 2(a). Obviously, the latter method discloses a substructure of several frequency steps at the discharge edge facing side of the wave field (0–10 mm), whereas the former only shows a decrease of the frequency.

To support the idea of cluster formation, the standard deviation of the frequency for all positions in the wave field was calculated using (5×5) pixel blocks. The corresponding map is displayed in Fig. 6(b) and reveals sharply defined boundaries

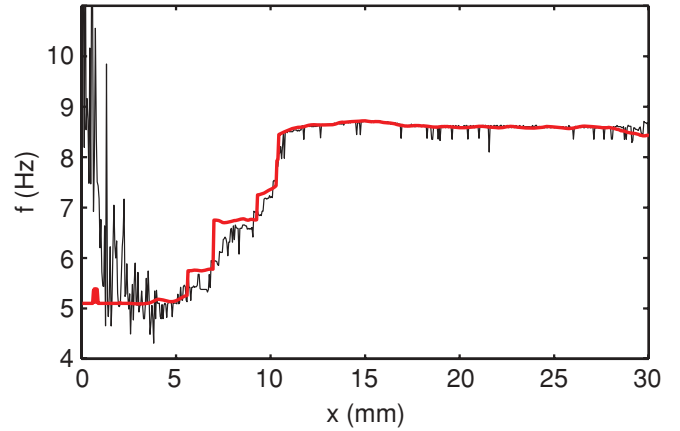


FIG. 7. (Color online) Frequency distribution determined from space-time diagram (fine black line) and from the temporal average of the instantaneous frequency (bold red line). The chosen horizontal axis is the same as in Fig. 2(a). The methods differ in the region of varying frequency (0–10 mm). The instantaneous frequencies disclose frequency steps in the intermediate region and a constant frequency at the discharge edge (0–5 mm).

between the clusters. Inside the clusters only small frequency variations are found.

C. Parameter variation

In order to investigate the behavior of frequency clusters under the influence of different plasma parameters, we compiled frequency maps for two more data sets. The first one was recorded at lower gas pressure and rf voltage compared to the exposed situation ($p = 15$ Pa, $U_{rf} = 48$ V_{pp}, $d = 9.55$ μ m) and is described in detail in Ref. [27]. The second data set was recorded at the same voltage but different pressure ($p = 15$ Pa, $U_{rf} = 70$ V_{pp}, $d = 6.8$ μ m), described in Ref. [33]. At first glance the former wave field is comparable to the exposed situation; the latter corresponds to a highly coherent wave state. The determined frequency maps with marked defect positions are shown in Fig. 8. Obviously, the first map has similarities with the exposed situation. In contrast, the map in Fig. 8(b) comprises just one large cluster. For each situation we calculated the modulation depth, defined as the ratio of signal maxima to signal minima, at those positions in the dust cloud where a sufficiently high wave activity was detected. We found an average ratio of 1.42 for the exposed situation of this paper, 1.52 for the measurement at low pressure and voltage, and 1.62 for the highly coherent state. In addition, the dust-density distribution for both states were estimated as described above. Since the profile of the first data set is qualitatively similar to the above exposed situation, only the distribution for the coherent state is shown in Fig. 9. Obviously, the estimated frequency gradients are 2–3 times lower compared to the other situations. Nevertheless, it is important to mention that the averaged intensity is only a rough estimate of the dust density, since inhomogeneous illumination may cause artifacts.

V. DEFECT STRUCTURES

Due to the fact that the wavelength of the DDWs varies significantly, the wave pattern is very complex. This results

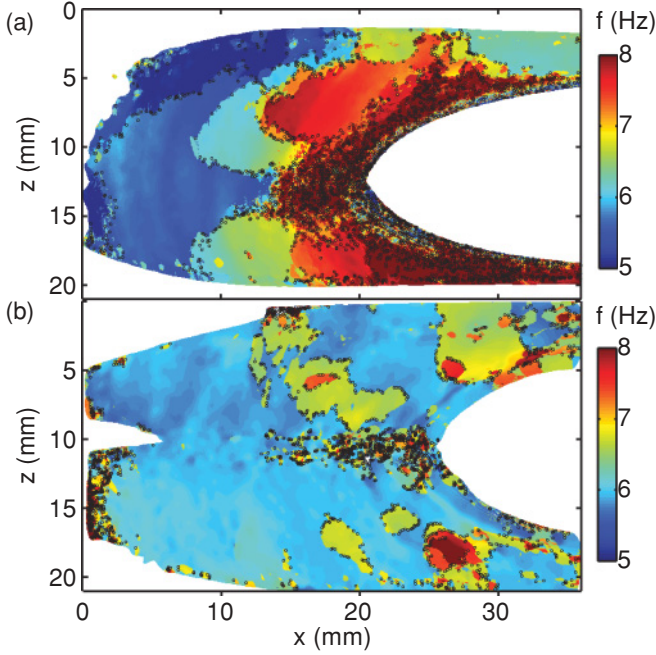


FIG. 8. (Color online) Frequency distributions for wave fields with modulation depths of (a) 1.52 and (b) 1.62. For the lower modulation depth the corresponding map reveals comparably small clusters and a high amount of topological defects. For the higher modulation depth one large cluster has formed.

in the occurrence of bifurcation points at positions where two wave fronts merge or split. Hence the conservation of wave number is not satisfied in the present system. As already seen in the space-time diagram, wave fronts are added to or removed from the system at the bifurcation. These particular points are called topological defects. To examine their relationship with the polychrome wave field, the defects are analyzed by utilizing the above compiled phase map (Fig. 5) that perfectly resembles the raw data.

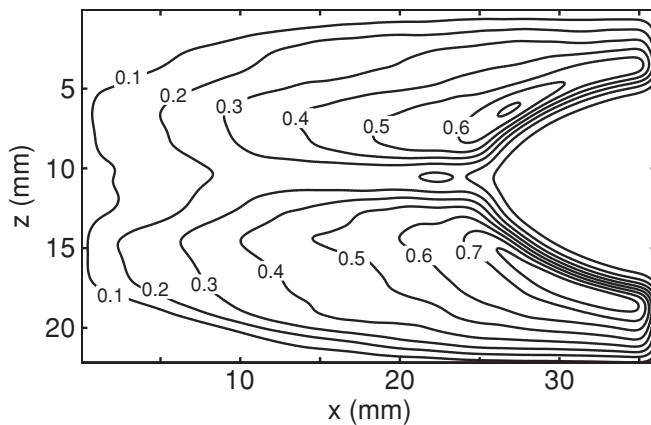


FIG. 9. Dust-density distribution for the wave field of Fig. 8(b) in arbitrary units, normalized to the maximum of the distribution. In comparison to the distribution of Fig. 3 only small gradients were found.

A. Defect analysis

In the unwrapped phase evolution, defects appear as abrupt jumps. One example occurs in the time series of Fig. 4(b). The detection of the spatial defect positions is based on the property that a defect can be regarded as a singularity in the phase map, i.e., the phase becomes undefined. To detect these phase defects, we derive from the instantaneous phase maps the so-called topological charge,

$$c(x, z, t) = \frac{1}{2\pi} \oint_{\Gamma} \vec{\nabla} \phi(x, z, t) \cdot d\vec{l}, \quad (4)$$

which was established by Nye [34] to evaluate singularities in ultrasonic waves. Since then it was applied in numerous works; see, e.g., Refs. [35,36]. The integral in Eq. (4) sums up infinitesimal phase differences $\vec{\nabla} \phi$ along a closed path Γ . Consequently, only those paths can contribute to the charge, which encircle a defect. This is illustrated in Fig. 10(a). It shows a closeup of the spatial phase information as determined by Eq. (3) at the vicinity of a defect. Two examples are given: path Γ_1 has its center on a wave front, whereas Γ_2 completely surrounds the defect. Only the charge of path Γ_2 differs from zero.

Applying the Stokes theorem, Eq. (4) allows us to define a topological charge density as [37]

$$c_d(x, z, t) = \frac{1}{2\pi} \cdot [\vec{\nabla} \times \vec{\nabla} \phi(x, z, t)]. \quad (5)$$

Using Eq. (5) is a more convenient way for determining the topological charge, as it reduces the computation time. The result is shown in Fig. 10(b). Since the vector field $\vec{\nabla} \phi$ was initially blurred with a Gaussian filter, the curl calculation yields a very smooth topological charge distribution. The charge that is assigned to the complete defect (integral over all pixels) takes values of +1 (white) or -1 (black), depending on the sense of rotation of the phase. In principle, also defects of higher orders, i.e., higher integers, are possible but do not appear in the evaluated data sets.

In a consecutive step, the defect positions can be determined with standard particle detection algorithms, like those introduced in Refs. [38,39]. The detection works with high accuracy because the topological charge of a defect has a Gaussian shape. In order to examine the relationship between frequency clusters and topological defects in the wave field, the positions of all defects are plotted on top of the frequency distribution of Fig. 6(a). This includes all defects that were found in the time series used for the frequency determination. It becomes evident that the defects appear almost exclusively at the boundaries between the frequency domains that were determined using the instantaneous frequency. The high amount of defects found near the void and in the outer regions of the wave field is due to irregular wave activity.

B. Defect dynamics

Since we have calculated the temporal evolution of the phase, it is also possible to track defect positions for a desired time interval, and thus an analysis of the dynamics of the defects could be performed. For this purpose, a sequence of successive frames of the topological charge is studied. The time step between two frames is given by the frame rate of

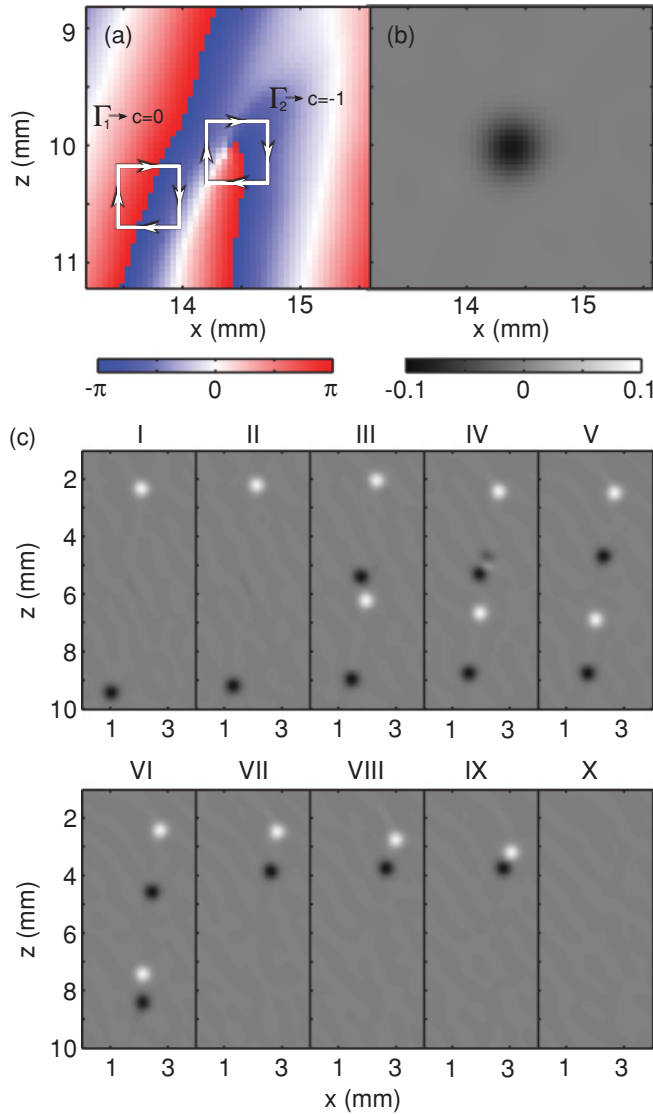


FIG. 10. (Color online) (a) The spatial phase information in the vicinity of a defect for the white square in Fig. 2(a). It marks the positions where two wave fronts merge into one. (b) Calculated topological charge density of the same region using Eq. (5). The charge of the defect results from the sum of all corresponding pixels and equals approximately -1 . (c) Evolution of a defect pair with opposite charge in the wave field. In frame III a new pair of defects is created. In frame VII the lower neighboring defects are annihilated; in frame X the upper pair is annihilated. The color bar is the same as in (b).

the camera as approximately $0.01 \mu s$. Since the defects are characterized by their charge, they can be treated as “particles.” Therefore the underlying pattern need not to be considered. An example for the motion of defect pairs with opposite charge is shown in Fig. 10(c). One remarkable feature of their motion is seen in frame III, where a second pair of defects between the original defects is created, resulting in four defects of alternating charge. Afterward, the two lower defects annihilate each other in frame VII; the upper pair vanishes in the last frame.

The observed events are in agreement with other experiments [40,41], which showed that defects are suddenly

occurring and disappearing objects. In addition, the defects are not fixed in the wave field and are consequently not moving with the local phase velocity. Instead, the wave front at a bifurcation that is located closer to the void is ruptured and caught up by the subsequent front, triggering a new rupture. In accordance to previous investigations [41,42], the defect motion can be separated into a “glide” motion (along the local wave velocity) and a “climb” motion (perpendicular to the local wave velocity). In our measurements the glide motion is dominant.

The defects represent events of vanishing amplitude as shown in Fig. 4(a), i.e., they are a consequence of destructively interfering waves and it is reasonable to assume that they move at the group velocity rather than the phase velocity. Unfortunately, the DDWs are characterized by their three-dimensional topology, so that defects may move out of the plane of observation. Consequently, a reliable estimation of all velocity components is not yet possible. This problem also implies that a detection of defect pairs of opposite topological charge, as seen in Fig. 10(c), at the ends of a wave front that is generated in the system is difficult. In principle, in three dimensions the defects will most probably occur along so-called “nodal lines” [43]. Nevertheless, the evaluation of long defect trajectories showed that they move with (70–90)% of the local phase velocity of the wave, which is in agreement with the above considerations.

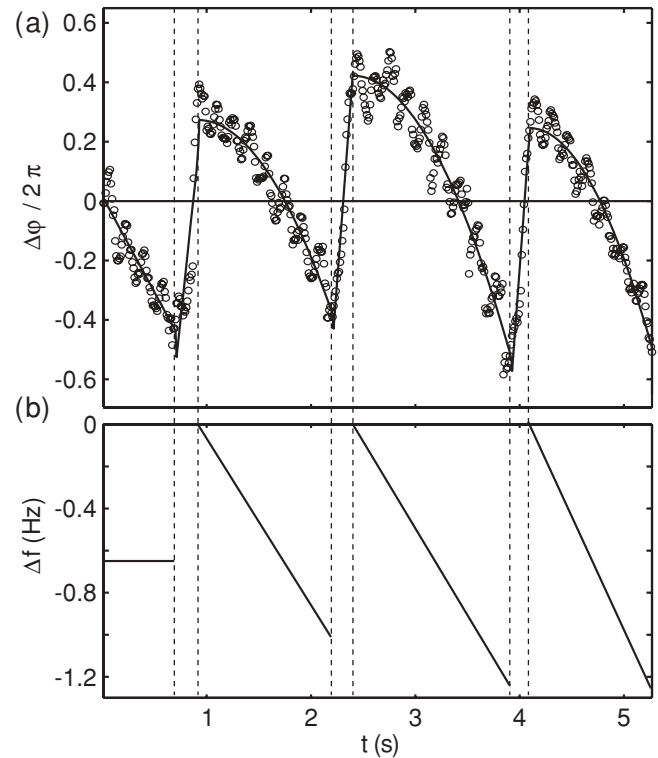


FIG. 11. (a) Evolution of $\Delta\phi(t) = \phi(t) - \bar{\phi}(t)$ (circles). The straight line corresponds to sectionwise parabolic fits between defects. (b) The derivative of the fitted curve in (a) transforms the phase differences into frequency differences. It shows a linear decrease between two defect events and is therefore a hint for a nonlinear interference.

C. Role of topological defects

The map of Fig. 6(b) illustrated that the frequency varies significantly only at the boundary between two adjacent clusters. These spatial variations are also seen as temporal fluctuations, which can be seen in Fig. 11(a). It shows a typical evolution of phase differences $\Delta\phi(t) = \phi(t) - \bar{\phi}(t)$ between instantaneous phase $\phi(t)$ and a time-averaged phase evolution $\bar{\phi}(t)$ that is determined by a linear fit on the unwrapped phase data. Due to the correction by a mean phase, $\Delta\phi(t)$ elucidates the behavior of the phase on a smaller time scale. In this particular example, a periodic pattern of defects appears, indicated by abrupt phase changes. Between these events the phase difference can be approximately described by a parabolic law. This evolution can be interpreted in terms of frequency differences by the temporal derivative of $\Delta\phi(t)$. Since this time series is affected by additional fluctuations due to the nonlinear character of the waves, a parabolic function is piecewise fitted to the data and differentiated afterwards. Figure 11(b) shows the resulting sawtoothlike deviation from instantaneous to mean frequency. This asymmetric evolution shows that the interference phenomenon that leads to the appearance of topological defects has a nonlinear character that is typical of relaxation oscillators. For a linear superposition of waves a sinusoidal variation would be expected. We have also observed defects with the opposite slope of the frequency evolution and an opposite sign of the phase jump.

VI. DISCUSSION

The observed dust-density waves show a very complicated wave pattern. The measured strong modulation depth proves the nonlinear character of the wave. The wave fronts are not strictly parallel but merge or split. These transient phenomena are known as topological defects. In principle, simple analysis methods, like the Fourier transform of the entire time series, allow us to determine a variety of wave properties. Nevertheless, the Fourier transform is an integrating method and thus has a time-averaging character with a frequency resolution determined by the length of the transform time series. Hence it is not capable to perform a suitable spatiotemporal analysis of the DDWs that includes the mentioned transient effects. Refined data analysis techniques adopted from digital signal processing, namely the Hilbert transform, made instantaneous physical quantities accessible. This means that the phase and amplitude of a wave can be determined with a resolution corresponding to the frame rate of the camera. The Hilbert transform allows a complete reconstruction of the spatiotemporal evolution of the wave field. We further defined an instantaneous frequency that makes it possible to study the frequency content of the waves in detail on different time scales. For example, one can evaluate the instantaneous frequency itself. Since the nonlinearity modulates the shape of the wave within one wave period, it is also possible to average the frequency over one wave period to remove such features. This allows a look at the specific behavior of the defects, as illustrated in Fig. 11(a). To get insight into the spatial frequency distribution of the waves, the frequency can further be averaged over several wave periods (at constant experimental conditions). The frequency analysis

based on the Hilbert transform is therefore similar to the wavelet transform, which also allows an adaptive control of the temporal resolution, but it is complementary to spectral methods like the Fourier transform.

The experimental data reveal the formation of frequency clusters that are separated by sharp boundaries. Besides a sharp transition in the frequency, the wave fronts show the aforementioned topological defects at boundaries between the clusters. This behavior was not expected because the system parameters inside the dust cloud, e.g., gas pressure, plasma potential, and particle charge, have smooth spatial variations with no abrupt changes. This suggests that the system undergoes synchronization processes within the clusters. The defects occur periodically in the wave field. Their repetition rate is proportional to the frequency step between two clusters. In our measurements, this periodicity cannot be determined at every position for two reasons. Since the cluster boundaries have a three-dimensional shape and the defects do not occur everywhere along a boundary [see Fig. 6(a)], the detection of defect events can be missed with the two-dimensional diagnostics. Furthermore, the defect boundaries in experimental situations are not sharp. They are broadened due to varying experimental parameters and noise [44]. Thus defects do not appear repeatedly at the same position, but fluctuate.

The formation of frequency clusters is known from other dynamical systems. There are a few experimental observations for purely one-dimensional systems. For example, spatially extended sections along the intestine of mammals were found to oscillate at a unique frequency [45]. In addition, frequency clustering was reported for the vortex shedding frequency in a flow behind cone-shaped bodies [46]. Our inspection of the existing literature on plasma waves has shown that, except for our recent investigations [27], the frequency clustering effect has not yet been reported in this field. Nevertheless, a number of numerical studies also showed this remarkable feature in the wave field. These simulations investigated the synchronization of arrays of mutually coupled nonlinear oscillators. The oscillators are subjected to a gradient of the natural frequency. The simulations cover chaotic Rössler oscillators [47], weakly nonlinear Ginzburg-Landau systems [48], and the Luo-Rudy model for cardiac cells [49].

It is important to mention that the synchronization of the individual oscillators is not only limited to an adjustment of their frequencies, but also of their phases. Otherwise a wave motion of oscillators, as found in our dusty plasma, would not be observable. Different simulations [49,50] showed that this leads to the formation of propagating wave patterns. In particular, it was shown that a system of integrate-and-fire oscillators exhibits wave motion [51], where the wave propagates from higher to lower frequencies, as observed in our experiment.

Our system of dust-density waves shows a similarity with the coupled oscillator models in that the size of the frequency clusters grows for increasing nonlinearity. This conclusion can be drawn since the modulation depth, which was determined for three different sets of parameters, can be interpreted as a measure for the degree of nonlinearity. Furthermore, the cluster size depends on the gradient of one of the system parameters, namely the dust-density distribution. This is also similar to

the models, where a gradient of the natural frequencies of the oscillators is included. The simulations reveal the appearance of topological defects at cluster boundaries [46,48] as was found in our experiments. It is found that the instantaneous frequency between two defect events decreases or increases linearly, which is similar to the periodic pulling effect of a driven van der Pol oscillator and describes a process where the oscillator frequency drifts toward the frequency of the driver, entrains for a short moment, and then changes abruptly [52].

Since the defect positions can be accurately determined with the applied analysis techniques, the investigation of the defect dynamics is possible. We observed the creation and annihilation of defect pairs with opposite topological charge, which might be a consequence of the complex three-dimensional defect motion.

Frequency clustering cannot be understood from linear wave properties. There, a wave maintains its frequency but matches the varying propagation speed by adjusting the wavelength. Rather, linear instability analysis shows that for the present wave phenomenon a range of wave modes becomes unstable, which suggests that the frequency clusters are associated with mutual synchronization of these modes.

VII. CONCLUSION

We explain the formation of frequency clusters as follows: Due to the high gas pressure in our experiment the damping rates are so strong that any disturbance of the dust density will be damped within a few millimeters. Consequently, the observed wave phenomena cannot be interpreted as propagating waves that are excited at one specific point in the dust volume. In fact, the system must gain energy everywhere in the wave field. This is true for DDWs since they are excited by streaming ions as a Buneman-type instability. They are therefore dominated by the local plasma parameters at an arbitrary position, as, e.g., by particle mass, particle charge, and dust density. Hence the dust volume may not be interpreted as a passive medium in which an externally excited wave propagates, but rather as an ensemble of oscillators with different dust-plasma frequencies, similar to an amplifying laser medium. Nevertheless, most other wave phenomena in the context of dusty plasmas are generated by an external driver, as, for example, Mach cone shocks [38] or shear waves [53], which are mediated by the force of a laser beam. These experiments were carried out in other parameter regimes, where the lower gas pressure allows a regular wave propagation. They are consequently not comparable to the present situation.

Due to nonuniform plasma conditions inside the discharge and a nonuniform dust distribution that decreases from the void edge to the outer regions of the discharge (see Fig. 3), a gradient of natural frequencies is established in the ensemble. It is not yet possible to identify the “oscillator” precisely. We conjecture that not a single particle but a bunch of particles with an extension in the order of a wavelength, which may penetrate each other, represent such individual oscillators. These oscillators interact mutually. Since the dust-density fluctuations show a high degree of modulation, we expect a strongly varying dust charge between wave crests and troughs, which causes the interaction to be nonlinear. Earlier investigations [54–57] showed that the van der Pol oscillator has a paradigmatic character for nonlinear plasma waves and may also be a suitable model for the observed DDWs.

As for the numerical simulations of Refs. [44,48], we expect the group of oscillators to synchronize each other over a certain distance, resulting in a common oscillation frequency. If the stress inside the ensemble becomes too strong, the synchronization breaks up and another cluster is formed. At the interface between two clusters, the occurrence of a topological defect is necessary to match the subgroups. The coherence length of the oscillators will then be given by the degree of nonlinearity and the dispersion of natural frequencies in the system. We could show that our dusty plasma revealed the same tendencies as the simulations.

It needs to be mentioned that the model in [48] assumes a diffusive, i.e., symmetric, coupling between the oscillators. However, in the present system, there is a unique wave propagation direction that may break this symmetry. Additionally, the authors modeled the oscillators via a complex Ginzburg-Landau equation, i.e., a weakly nonlinear version of the van der Pol equation, which might also be more suitable for our system.

In conclusion, our investigations lead to a different view on dust-density waves where the wave field is treated as an ensemble of mutually coupled self-excited nonlinear oscillators. This is a possible explanation for the observed formation of frequency clusters and the occurrence of topological defects at the cluster boundaries.

ACKNOWLEDGMENTS

This work was supported by DLR under Contract No. 50WM0739 and the European Space Agency and in part by Sonderforschungsbereich Contract No. TR-24 A2. The authors thank I. Pilch and T. Bockwoldt for fruitful discussions. The expert technical assistance by V. Rohwer and M. Poser is gratefully acknowledged.

-
- [1] A. Barkan, R. L. Merlino, and N. D’Angelo, *Phys. Plasmas* **2**, 3563 (1995).
 - [2] C. Thompson, A. Barkan, N. D’Angelo, and R. L. Merlino, *Phys. Plasmas* **4**, 2331 (1997).
 - [3] S. V. Ratynskaia, M. Kretschmer, S. A. Khrapak, R. A. Quinn, G. E. Morfill, M. H. Thoma, A. V. Zobnin, A. D. Usachev, O. Petrov, and V. E. Fortov, *IEEE Trans. Plasma Sci.* **32**, 613 (2004).
 - [4] T. Trottenberg, D. Block, and A. Piel, *Phys. Plasmas* **13**, 042105 (2006).
 - [5] E. Thomas Jr., *Phys. Plasmas* **13**, 042107 (2006).
 - [6] J. D. Williams, E. Thomas Jr., and L. Marcus, *Phys. Plasmas* **15**, 043704 (2008).
 - [7] E. Thomas Jr., *Phys. Plasmas* **17**, 043701 (2010).
 - [8] J. B. Pieper and J. Goree, *Phys. Rev. Lett.* **77**, 3137 (1996).

- [9] L.-W. Teng, M.-C. Chang, Y.-P. Tseng, and L. I, *Phys. Rev. Lett.* **103**, 245005 (2009).
- [10] A. Piel, M. Klindworth, O. Arp, A. Melzer, and M. Wolter, *Phys. Rev. Lett.* **97**, 205009 (2006); **99**, 209903(E) (2007).
- [11] A. Piel, O. Arp, M. Klindworth, and A. Melzer, *Phys. Rev. E* **77**, 026407 (2008).
- [12] S. A. Khrapak, D. Samsonov, G. E. Morfill, H. Thomas, V. Yaroshenko, H. Rothermel, V. Fortov, A. Nefedov, V. Molotkov, O. Petrov, A. Lipaev, A. Ivanov, and Y. M. Baturin, *Phys. Plasmas* **10**, 1 (2003).
- [13] V. V. Yaroshenko, B. M. Annaratone, S. A. Khrapak, H. M. Thomas, G. E. Morfill, V. E. Fortov, A. M. Lipaev, V. I. Molotkov, O. F. Petrov, A. I. Ivanov, and M. V. Turin, *Phys. Rev. E* **69**, 066401 (2004).
- [14] M. Rosenberg, *J. Vac. Sci. Technol. A* **14**, 631 (1996).
- [15] P. K. Shukla, *Phys. Plasmas* **10**, 1619 (2003).
- [16] M. Schwabe, M. Rubin-Zuzic, S. Zhdanov, H. M. Thomas, and G. E. Morfill, *Phys. Rev. Lett.* **99**, 095002 (2007).
- [17] M. Schwabe, S. K. Zhdanov, H. M. Thomas, A. V. Ivlev, M. Rubin-Zuzic, G. E. Morfill, V. I. Molotkov, A. M. Lipaev, V. E. Fortov, and T. Reiter, *New J. Phys.* **10**, 033037 (2008).
- [18] J. Heinrich, S.-H. Kim, and R. L. Merlino, *Phys. Rev. Lett.* **103**, 115002 (2009).
- [19] O. Arp, D. Caliebe, K. Menzel, A. Piel, and J. Goree, *IEEE Trans. Plasma Sci.* **38**, 842 (2010).
- [20] N. N. Rao, P. K. Shukla, and M. Y. Yu, *Planet. Space Sci.* **38**, 543 (1990).
- [21] P. Kaw and R. Singh, *Phys. Rev. Lett.* **79**, 423 (1997).
- [22] S. V. Singh and N. N. Rao, *Phys. Plasmas* **5**, 94 (1998).
- [23] V. E. Fortov, A. G. Khrapak, S. A. Khrapak, V. I. Molotkov, A. P. Nefedov, O. F. Petrov, and V. M. Torchinsky, *Phys. Plasmas* **7**, 1374 (2000).
- [24] A. Zobnin, A. Usachev, O. Petrov, and V. Fortov, *J. Exp. Theor. Phys.* **95**, 429 (2002).
- [25] S. A. Khrapak and V. V. Yaroshenko, *Phys. Plasmas* **10**, 4616 (2003).
- [26] I. Pilch, T. Reichstein, and A. Piel, *Phys. Plasmas* **16**, 123709 (2009).
- [27] K. O. Menzel, O. Arp, and A. Piel, *Phys. Rev. Lett.* **104**, 235002 (2010).
- [28] M. Klindworth, O. Arp, and A. Piel, *J. Phys. D* **39**, 1095 (2006).
- [29] G. E. Morfill, H. M. Thomas, U. Konopka, H. Rothermel, M. Zuzic, A. Ivlev, and J. Goree, *Phys. Rev. Lett.* **83**, 1598 (1999).
- [30] M. Mikikian, L. Coudel, M. Cavarroc, Y. Tessier, and L. Boufendi, *New J. Phys.* **9**, 268 (2007).
- [31] D. Gabor, *J. Inst. Electr. Eng.* **93**, 429 (1946).
- [32] A. S. Pikovsky, M. Rosenblum, and J. Kurths, *Synchronization: A Universal Concept in Nonlinear Science* (Cambridge University Press, Cambridge, England, 2001).
- [33] K. Menzel, O. Arp, D. Caliebe, and A. Piel, *IEEE Trans. Plasma Sci.* **38**, 838 (2010).
- [34] J. F. Nye and M. V. Berry, *Proc. R. Soc. London, Ser. A* **336**, 165 (1974).
- [35] A. La Porta and C. M. Surko, *Phys. Rev. E* **53**, 5916 (1996).
- [36] M.-A. Bray and J. P. Wikswo, *IEEE Trans. Biomed. Eng.* **47**, 1086 (2002).
- [37] F. S. Roux, *Opt. Commun.* **268**, 15 (2006).
- [38] D. Samsonov, J. Goree, H. M. Thomas, and G. E. Morfill, *Phys. Rev. E* **61**, 5557 (2000).
- [39] Y. Feng, J. Goree, and B. Liu, *Rev. Sci. Instrum.* **78**, 053704 (2007).
- [40] A. La Porta and C. M. Surko, *Phys. Rev. Lett.* **77**, 2678 (1996).
- [41] K. E. Daniels and E. Bodenschatz, *Chaos* **13**, 55 (2003).
- [42] A. La Porta and C. M. Surko, *Physica D* **139**, 177 (2000).
- [43] M. R. Dennis, *New J. Phys.* **5**, 134 (2003).
- [44] T. E. Vadivasova, G. I. Strelkova, and V. S. Anishchenko, *Phys. Rev. E* **63**, 036225 (2001).
- [45] N. E. Diamant and A. Bortoff, *Am. J. Physiol.* **216**, 301 (1969).
- [46] B. R. Noack, F. Ohle, H. Eckelmann, *J. Fluid Mech.* **227**, 293 (1991).
- [47] G. V. Osipov, A. S. Pikovsky, M. G. Rosenblum, and J. Kurths, *Phys. Rev. E* **55**, 2353 (1997).
- [48] G. V. Osipov and M. M. Sushchik, *Phys. Rev. E* **58**, 7198 (1998).
- [49] O. I. Kanakov, G. V. Osipov, C.-K. Chan, and J. Kurths, *Chaos* **17**, 015111 (2007).
- [50] A. K. Kryukov, G. V. Osipov, A. V. Polovinkin, and J. Kurths, *Phys. Rev. E* **79**, 046209 (2009).
- [51] P. C. Bressloff and S. Coombes, *Phys. Rev. Lett.* **80**, 4815 (1998).
- [52] M. E. Koepke and D. M. Hartley, *Phys. Rev. A* **44**, 6877 (1991).
- [53] V. Nosenko, J. Goree, and A. Piel, *Phys. Rev. Lett.* **97**, 115001 (2006).
- [54] T. Klinger, A. Piel, F. Seddighi, and C. Wilke, *Phys. Lett. A* **182**, 312 (1993).
- [55] M. E. Koepke, T. Klinger, F. Seddighi, and A. Piel, *Phys. Plasmas* **3**, 4421 (1996).
- [56] H. Klostermann, A. Rohde, and A. Piel, *Phys. Plasmas* **4**, 2406 (1997).
- [57] D. Block, A. Piel, C. Schröder, and T. Klinger, *Phys. Rev. E* **63**, 056401 (2001).